Generation of Perfect Electron Vortex Beam with a Customized Beam Size Independent of Orbital Angular Momentum

Ruixuan Yu, Pengcheng Huo, Mingze Liu, Wenqi Zhu, Amit Agrawal, Yan-qing Lu,* and Ting Xu*

Read Online

ACCESS | Metrics & More | Article Recommendations | Supporting Information

ABSTRACT: The electron vortex beam (EVB)-carrying quantized orbital angular momentum (OAM) plays an essential role in a series of fundamental research. However, the radius of the transverse intensity profile of a doughnut-shaped EVB strongly depends on the topological charge of the OAM, impeding its wide applications in electron microscopy. Inspired by the perfect vortex in optics, herein, we demonstrate a perfect electron vortex beam (PEVB), which completely unlocks the constraint between the beam size and the beam's OAM. We design nanoscale holograms to generate PEVBs carrying different quanta of OAM but exhibiting almost the same beam size. Furthermore, we show that the beam size of the PEVB can be readily controlled by only modifying the design parameters of the hologram. The generation of PEVB with a customized beam size independent of the OAM can promote various *in situ* applications of free electrons carrying OAM in electron microscopy.

KEYWORDS: *Electron vortex beam, orbital angular momentum, hologram, nanostructure*
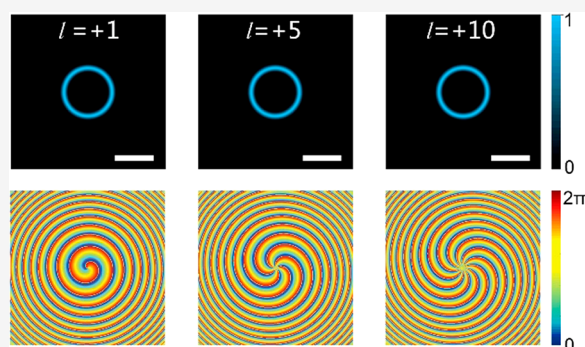
The wave-like behavior of electrons can be described as a complex-value wave function whose degrees of freedom corresponding to the radial and azimuthal indices determine their spatial structure.[1] By controlling these parameters and leveraging recent advances in nanofabrication and electron microscopy techniques, remarkable progress has been realized toward generating structured electron beams with tailored wave packets including the electron vortex beam (EVB),[2−12] electron Hermite−Gaussian beam,[13,14] electron Airy beam,[15,16] and electron Bessel beam.[17−19] Particularly, the generation of EVBs in free space has garnered considerable attention owing to their potential to extend the functionalities of electron microscopy.[20]

Considering the formal equivalence of the Schrödinger and paraxial Helmholtz equations, analogous to the optical vortex,[21−28] the electron vortex can be derived from a Laguerre−Gaussian-form solution and exists in a freely propagating electron beam.[4] In polar coordinates (ρ, ϕ), the form of a conventional EVB at the transverse plane is expressed as[2,3]

$$\Psi(\rho, \phi) \propto G(\rho) L_p^{|l|} \left[\frac{\sqrt{2}\rho}{\omega_0} \right]^{|l|} e^{il\phi} \qquad (1)$$

where $G(\rho)$ is the Gaussian function, $L_p^{|l|}$ is the generalized Laguerre polynomial, l is the topological charge, p is the radial index, and w_0 is the beam waist. The wave function in eq 1 describes an EVB possessing a helical wavefront that carries a quantized OAM of $l\hbar$ (i.e., $\hbar$ is the reduced Planck's constant)

in free space. The transverse intensity distribution, $|\Psi|^2$, of an EVB exhibits a characteristic doughnut-shaped annular profile. Various techniques, such as using nanostructured materials[4−8] and electrostatic elements,[11,12] have been employed to generate EVBs; in all cases, the beam radius is proportional to the topological charge $|l|$. This dependence is nonideal for electron microscopy applications that require illumination of EVBs with a different OAM values (for example, in quantitatively detecting transition radiation[29] or probing chiral plasmon resonances[30]). Although other approaches, such as changing the EVB generator's footprint or the electron's acceleration voltage (i.e., equivalent to changing the electron wavelength), can slightly adjust the size of the EVB, they can also increase the complexity of the experimental setup and have a limited scope of applications. Similarly, the above characteristic of EVB exists in an optical vortex beam.[28] In the field of optics, the concept of a perfect optical vortex beam has been proposed to overcome this limitation by implementing Fourier transformation on a Bessel beam.[31] Based on this approach, perfect optical vortex beams with ring radii independent of the topologic charges have been successfully
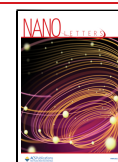
generated using spatial light modulators[31−33] or photonic metasurfaces comprising subwavelength nanostructures.[34−36] However, this unique vortex beam has not been demonstrated for electron waves because the generation methods used in optics are inappropriate to be analogously adopted for modulating electron beams due to the very short de Broglie wavelength of electrons, typically in picometer scales.

Herein, inspired by the concept of a perfect optical vortex beam, we experimentally demonstrate the generation of perfect electron vortex beams (PEVBs) using nanoscale diffraction holograms. Mathematically, an ideal PEVB can be defined as an electron beam possessing a complex transverse amplitude satisfying the following equation:

$$\Psi(\rho, \phi) = \delta(\rho - \rho_0)e^{il\phi} \qquad (2)$$

where $\delta(\rho - \rho_0)$ is the Dirac delta function and ρ_0 is the radius of the EVB. Eq 2 is exactly of Bessel form in Fourier space (see details in Supplementary Note 1). The Bessel beam is a well-known solution to the Helmholtz equation of photons or the Schrödinger equation of electrons in free space.[37−39] Therefore, the PEVB can be generated in Fourier space by implementing a Fourier transform on an electron Bessel beam in real space, where the functionality of the Fourier transform can be realized by using the magnetic lens in a transmission electron microscopic (TEM) column. Unfortunately, it is impossible to experimentally produce an ideal electron Bessel beam with infinite energy or, equivalently, a Dirac delta field. Therefore, hereinafter, we only consider a finite electron Bessel beam expressed as a Bessel wave packet multiplied with a Gaussian function expressed in cylindrical coordinates (r, θ, z):[40]

$$\Phi(r, \theta, z) = e^{-r^2/\omega_0^2} J_l(k_r r)e^{ik_z z}e^{il\theta} \qquad (3)$$

where k_r and k_z are the radial and longitudinal wave vectors that are confined by $k = \sqrt{k_r^2 + k_z^2} = 2\pi/\lambda_{dB}$, k is the magnitude of the free electron's wave vector, and λ_{dB} is the de Broglie electron wavelength. After the electron Bessel−Gaussian beam propagates through a magnetic lens of focal length f, the transmitted wave packet at the back focal plane with a beam waist, ω_f is derived using a standard integral and Bessel function identity (see Supplementary Note 2):

$$\Psi(\rho, \phi) = \frac{\omega_0 i^{l-1}}{\omega_f}e^{-(\rho-\rho_0)^2/\omega_f^2}e^{il\phi} \qquad (4)$$

From eq 4, it is evident that the PEVB's transverse intensity distribution, $|\Psi|^2$, is shaped by a Gaussian profile with a maximum at $\rho = \rho_0$. Radius ρ_0 is independent of topological charge and can be expressed as $\rho_0 = f \sin \theta_\rho$, where $\theta_\rho = \arcsin(k_r/k)$ is the diffractive polar angle of the electrons. For example, Figure 1a presents the calculated transverse intensity and phase distribution of the proposed PEVBs carrying different OAMs ($l = +1$, $+5$, and $+10$) at the focal plane. As expected, these PEVBs are characterized by a thin annular intensity distribution along their boundary, and their radii are independent of the topological charge. Compared with our work, the finite electron Bessel beam used for the Fourier transform in ref 41 has few radial modes, which would not satisfy the condition required for the generation of PEVB.

We use a binary phase modulation hologram[15,17,42] composed of nanoscale forked gratings to produce a higher-
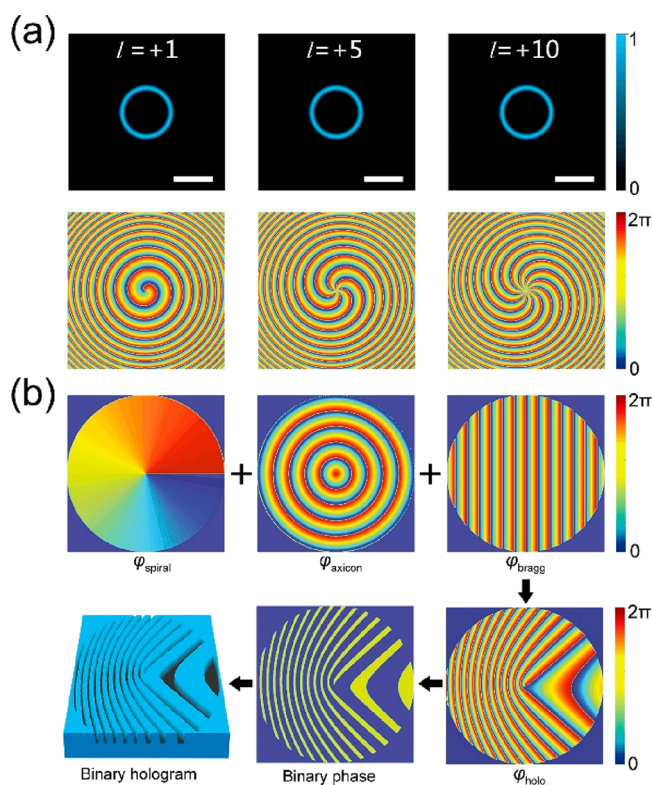

Figure 1. (a) Calculated transverse intensity (top panels) and phase (bottom panels) distributions of proposed perfect electron vortex beams (PEVBs) with topological charges of $l = +1$, $+5$, and $+10$ at the focal plane. Scale bars: 5 μrad. (b) Design flow of binary phase holograms for generating a higher-order electron Bessel−Gaussian beam.

order Bessel−Gaussian beam and employ a magnetic lens to perform a Fourier transform to generate a PEVB carrying an arbitrary OAM (see Figure S1). The binary phase mask can impart a transverse composite phase profile $\varphi_{holo}(r,\theta)$, which is the superposition of a spiral phase $\varphi_{spiral}(\theta)$, axicon focusing phase $\varphi_{axicon}(r)$, and Bragg carrier phase $\varphi_{Bragg}(r,\theta)$ to the incident electron beam, which are shown in the Figure 1b (see details in Supplementary Note 3). The spiral phase term and axicon focusing phase term control the topological charge and ring radius of the PEVB, respectively. The Bragg carrier phase term can separate different diffraction orders and avoid crosstalk between them. According to phase term $\varphi_{holo}(r,\theta)$, the holographic masks can be constructed using the following equation:

$$H(r, \theta) = \frac{1}{2}H_0\left\{\text{sgn}\left[\cos\left(l\theta - \frac{2\pi}{T}r + \frac{2\pi}{\Lambda}r\cos\theta\right) + D\right] + 1\right\} \qquad (5)$$

where H_0 is the height of holographic grating, sgn is the sign function, D is a duty cycle (the ratio of one grating spine' width to one grating period), $T = 2\pi/k_r$ is the axicon period and controls the electron Bessel−Gaussian beam, and Λ is the carrier period.

We design and fabricate three masks (Figure 2a) with the hologram parameters of axicon period $T = 800$ nm and carrier period of $\Lambda = 200$ nm. The fork dislocations in the holograms indicate that the encoded topological charge numbers are $|l| = 1$, 5, and 10 (see the insets in Figure 2a). A field emission gun TEM (FEG-TEM) is used to experimentally characterize the
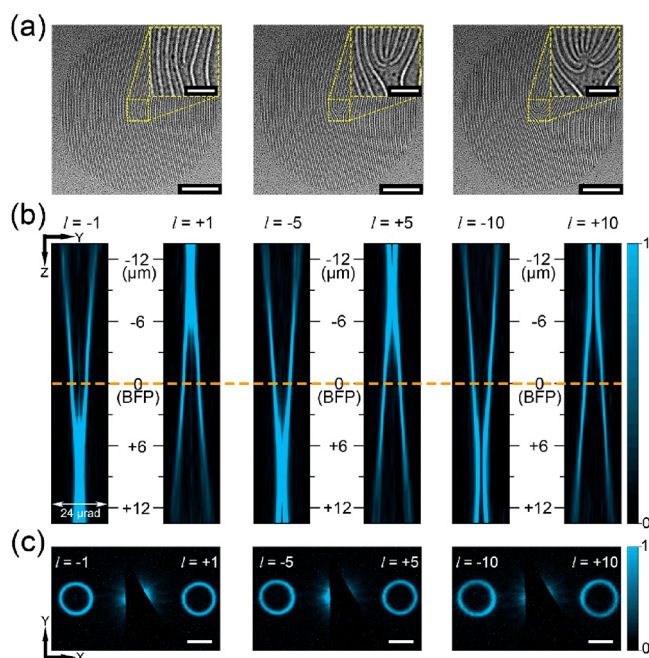
Figure 2. (a) Transmission electron microscopic (TEM) images of three fabricated nanoscale holograms encoding different amounts of topological charges of $|l|$ = 1, 5, and 10. Scale bars: 2 μm. Insets are the enlarged middle portions of TEM images. Scale bars: 500 nm. (b) Recorded intensity distribution of generated electron vortex beams for three holograms corresponding to +1 and −1 orders in the $y-z$ plane. (c) Recorded annular intensity profiles of six generated electron vortices corresponding to +1 and −1 orders at the back focal plane (depicted by the orange dashed lines in panel b). Scale bars: 5 μrad.

performance of the fabricated devices. The transverse intensity distributions of the generated PEVBs are recorded along the propagation direction (z-axis) at a nominal step of ≈1.5 μm. Figure 2b displays the intensity distribution of the generated PEVBs (+1 and −1 diffraction orders) along the $y-z$ plane by stitching all the captured $x-y$ plane images together. For the +1 order (right panels of Figure 2b), three diffracted PEVBs with different topological charges of l = +1, +5, and +10 exhibit almost identical beam radii and beam divergences. Due to the diffraction property of the binary phase mask, the PEVBs of the −1 diffraction order predictably possess opposite topological charges of l = −1, −5, and −10. Additionally, their spatial intensities and beam divergences in the $y-z$ plane (left panels of Figure 2b) show mirror symmetry with respect to the +1 diffraction order, implying that PEVBs of positive order are complex conjugates of the negative order. The radii of PEVBs for the +1 order become larger as the distance z increases from the back focal plane, signifying that the PEVB generated in Fourier space no longer has nondiffracting features (see details in Supplementary Note 4). Moreover, the spatial intensity distribution of PEVB is of conical shape, which looks similar to the conical illumination in a scanning transmission electron microscope (STEM). Nevertheless, compared with conical illumination, the PEVB has a helical phase wavefront and possesses an OAM, which may be used to further extend the functionality of STEM. Figure 2c shows the recorded annular intensity distributions of PEVBs at the back focal plane. As expected, the intensity profiles for six electron vortices are nominally identical. To quantitatively analyze the size of PEVBs, the cross sections of in-plane intensity profiles along

the y-direction are shown in Figure S2. The diffracted polar angle can instead substitute the radii of the electron vortices, θ_ρ, owing to the relatively constant focal length of the Fourier transform lens during measurements. The measured θ_ρ of electron vortices are (3.08 ± 0.08) μrad for l = +1, (3.21 ± 0.07) μrad for l = +5, and (3.35 ± 0.07) μrad for l = +10. The uncertainties are standard deviations for repeated measurements. Although these experimental results are all close to the designed value of θ_ρ = 3.14 μrad, their beam radii are not identical. This is because the binary phase mask with small aperture size leads to the generation of a quasi-Gaussian−Bessel beam rather than a standard Gaussian−Bessel beam. To further explore the aperture size effect on the generation of PEVBs, the results for the Fourier transform of the binary phase masks with different aperture sizes are calculated and compared with the results for the Fourier transform of the standard Gaussian−Bessel beams with different beam sizes, which are shown in the Figure S4 (see details in Supplementary Note 5). The hologram-generated PEVBs with different topological charges can have almost identical beam radius if the aperture size of the binary phase mask is large enough.

Additionally, we record the interference patterns at the back focal plane without the Bragg carrier phase term imparted on the holograms (Figure S5). As the generated electron vortices of ±1 diffraction order are complex conjugates, the recorded petal-like annular pattern has a lobe number of $|2l|$. The topological charge of the generated PEVBs can be directly distinguished from the lobe number of petal-like interference patterns, further validating the designed topological charge numbers 1, 5, and 10. For comparison, we also fabricate three holograms with the same footprints to generate conventional EVBs with identical topological charges (Figure S6a). The measured transverse intensity distributions of these EVBs at the focal plane are given in Figure S6b. Indeed, the diffracted polar angle, θ_ρ, rapidly grows from (0.34 ± 0.06) μrad for l = +1 to (1.31 ± 0.07) μrad for l = +10, confirming that the radius of conventional EVB is proportional to the magnitude of topological charge. Subsequently, we calculate the growth factor η of the radii of two-electron vortices with topological charges of l = +1 and l = +10 as $\eta = (\theta_{\rho,l=10} - \theta_{\rho,l=1})/\theta_{\rho,l=1}$. For conventional EVB, $\eta \approx 285.3\%$, whereas for PEVB, $\eta \approx 8.7\%$. These results clearly indicate that the radii of PEVBs generated by the proposed approach are nominally insensitive to the topological charge number.

Next, we leverage this unique characteristic to demonstrate the superposition of PEVBs with different OAMs. Here, considering two PEVBs with topological charges of l_1 and l_2, the complex amplitude of the superposed electron vortices can be expressed as $U = \Psi_{l_1} + \Psi_{l_2}$, whose transverse intensity profile should exhibit a petal-like annular pattern with $|l_1 - l_2|$ lobes due to interference between the two PEVBs. The morphology of the nanoscale hologram mask fabricated for creating a superposed state of electron vortices is determined by the product of transmission phase functions of the two binary phase holograms. We fabricate three hologram masks to generate three different superposed electron vortices (U_1, U_2, and U_3). The TEM images of fabricated holograms are shown in Figure S7. The states of U_1, U_2, and U_3 are the superpositions of PEVBs with different topological charges corresponding to $U_1 = \Psi_{l_1=+1} + \Psi_{l_2=-5}$, $U_2 = \Psi_{l_1=+1} + \Psi_{l_2=-10}$, and $U_3 = \Psi_{l_1=+5} + \Psi_{l_2=-10}$, respectively. The transverse

intensity distributions of the three states at the back focal plane are shown in the left panels of Figure 3a−c. As expected, the
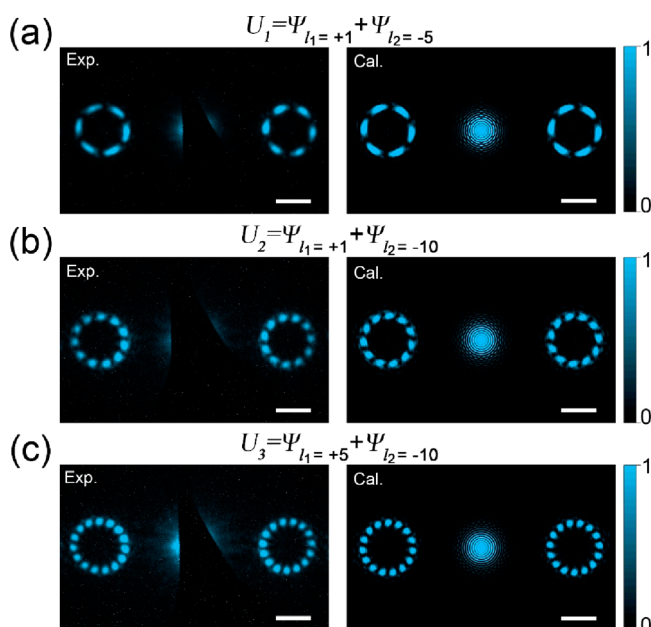

Figure 3. (a−c) Results of the three superpositions U_1, U_2, and U_3 of different PEVBs with topological charges $l_1 = +1$ and $l_2 = -5$, $l_1 = +1$ and $l_2 = -10$, and $l_1 = +5$ and $l_2 = -10$, respectively. Left panels: experimental results. Right panels: calculation results. Scale bars: 5 μrad.

measured intensity distribution of U_1, U_2, and U_3 exhibits petal-like annular patterns with 6, 11, and 15 lobes, respectively. Moreover, the edge contours of the patterns are of identical size owing to the radii-independent topological charge characteristic of PEVBs. The experimental results presented are consistent with the expected theoretical predictions (right panels of Figure 3). Notably, the superposition of conventional EVBs at the focal plane with considerably different topological charge numbers cannot be realized due to the significant difference in their sizes (Figure S6b). The PEVB obtained using the holographic reconstruction technique presents a simple and elegant avenue for generating a superposition of electron vortex states carrying different quantized OAM values.

Finally, unlike the conventional EVB, the PEVB radius can be arbitrarily controlled by only modifying the axicon factor of the hologram mask without changing the device footprint or the acceleration voltage of the electron. To illustrate this, we designed and fabricated two groups of hologram masks with the same footprints but different axicon periods: $T = 1,200$ and 400 nm, respectively. Each group was encoded with three different topological charge numbers of $|l| = 1$, 5, and 10 (Figure S8). The transverse intensity distributions of the PEVBs for the ±1 diffraction order at the back focal plane are shown in the right panels of Figure 4a and b. For each group, the intensity profiles of PEVBs carrying different OAM values are considerably similar and agree with the calculated results shown in Figure S9. The cross sections of in-plane intensity profiles extracted from Figure 4a and b along the y-direction are shown in Figure S10. For these two groups, the values for θ_ρ were measured as follows: for $T = 1200$ nm, $\theta_\rho = (2.08 \pm 0.08)$ μrad for $l = +1$, $\theta_\rho = (2.17 \pm 0.09)$ μrad for $l = +5$, and
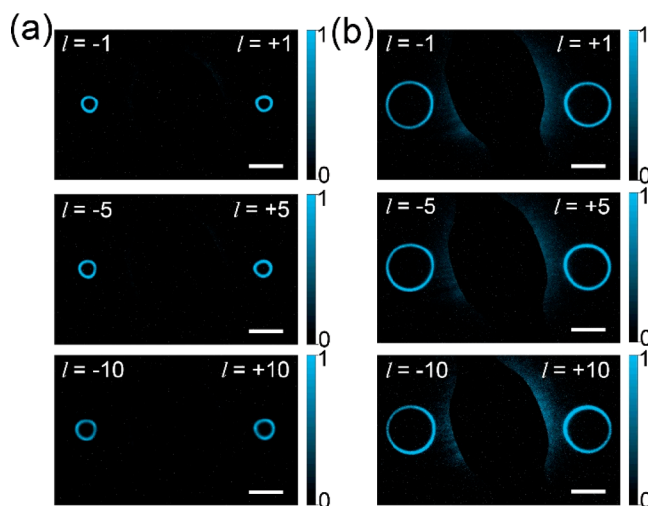

Figure 4. Results of holograms with (a) $T = 1200$ nm and (b) $T = 400$ nm for generating different PEVBs with two types of predesigned beam diameters and topological charge number of $|l| = 1$, 5, and 10. Scale bars: 10 μrad.

$\theta_\rho = (2.46 \pm 0.08)$ μrad for $l = +10$; for $T = 400$ nm, $\theta_\rho = (6.09 \pm 0.07)$ μrad for $l = +1$, $\theta_\rho = (6.16 \pm 0.09)$ μrad for $l = +5$, and $\theta_\rho = (6.44 \pm 0.08)$ μrad for $l = +10$. These experimental results are close to the theoretically predicted values of $\theta_\rho = 2.09$ μrad for $T = 1,200$ nm and $\theta_\rho = 6.28$ μrad for $T = 400$ nm. The growth factors η of two types of PEVBs with $l = +1$ and $l = +10$ were calculated as $\eta \approx 18.3\%$ for $T = 1,200$ nm and $\eta \approx 5.7\%$ for $T = 400$ nm, which were much less than the conventional EVB growth factor. The ability to control the beam size through simple design modification further enhances the usability of the proposed PEVB.

In conclusion, we experimentally demonstrate the generation and manipulation of PEVB, whose ring radius is independent of the OAM. By designing nanoscale holographic masks, we create and observe PEVBs with different quanta of OAM but constant radii. As the electron OAM beam possessing charges can interact with external fields, they can be potentially applied to perform various fundamental physics studies via an electron microscope. Some applications include quantitatively measuring a nanoscale out-of-plane magnetic field with large OAM values,[43,44] probing plasmon resonances and chiral biomolecule with OAM-induced dichroism,[14,30] and observing the weak polarization radiation produced by electron beams with high OAM values.[45] In contrast to the traditional EVB, the PEVB with a controllable radius may offer a convenient and simple method for generating a free-electron Landau state.[46] Furthermore, the "OAM-unbalanced" superposition of PEVBs with a considerable difference between their nonzero topological charge numbers can be successfully generated with smaller distortions, which might be used to study the various Gouy rotations of different EVB superpositions and improve the measurement accuracy of its Gouy rotation angle.[47] Moreover, we envision that the PEVB may be used to study electron spin−orbit coupling in the relativistic regime.[48−50]

■ METHODS

Sample Preparation. The binary phase holographic grating masks are designed and fabricated on 100 nm-thick silicon nitride membranes using focused ion beam (FIB)

milling. The FIB tool utilizing Ga-ions is operated at an acceleration voltage of 30 keV and ion beam current of 7.7 pA. The patterning is performed with a minimum step size of 4 nm and a dwell time of 0.42 ms. The milling is performed over an area of $8.5 \times 8.5 \ \mu m^2$ for each grating.

TEM Measurement. The evolution of EVB is observed using a Tecnai TF20 FEG-TEM, producing a relatively coherent monoenergetic electron beam with an energy of 200 keV, corresponding to the relativistic de Broglie wavelength of ~2.51 pm. The holographic grating masks are placed at the front focal plane of the magnetic objective lens, which can perform the Fourier transforms of the hologram-generated finite electron Bessel beams. The diffraction patterns are recorded at a FEG-TEM low-angle diffraction mode (LAD), for which the magnetic objective lens is operated at a low current. The LAD mode enables long camera length; hence, a polar angle of diffraction for electrons <1 μrad can be measured. A charge-coupled device camera, along with another magnetic lens system, is used to capture the propagation dynamics of the generated EVB. Relationship between current and defocusing distance of the magnetic objective lens in LAD mode can be determined by Bragg diffraction experiment in TEM.[15,51] Thus, we can estimate the z-axis spacing distance between each recorded image of the generated PEVB.

ASSOCIATED CONTENT

SI Supporting Information

The Supporting Information is available free of charge at https://pubs.acs.org/doi/10.1021/acs.nanolett.2c03822.

> Theoretical derivation of electron vortex beam, design of binary phase holograms, propagation properties of electron vortex beam (PDF)

AUTHOR INFORMATION

Corresponding Authors

Ting Xu − *National Laboratory of Solid-State Microstructures and Collaborative Innovation Center of Advanced Microstructures, Nanjing University, Nanjing 210093, China; College of Engineering and Applied Sciences and Jiangsu Key Laboratory of Artificial Functional Materials, Nanjing University, Nanjing 210093, China;* orcid.org/0000-0002-0704-1089; Email: xuting@nju.edu.cn

Yan-qing Lu − *National Laboratory of Solid-State Microstructures and Collaborative Innovation Center of Advanced Microstructures, Nanjing University, Nanjing 210093, China; College of Engineering and Applied Sciences and Jiangsu Key Laboratory of Artificial Functional Materials, Nanjing University, Nanjing 210093, China;* orcid.org/0000-0001-6151-8557; Email: yqlu@nju.edu.cn

Authors

Ruixuan Yu − *National Laboratory of Solid-State Microstructures and Collaborative Innovation Center of Advanced Microstructures, Nanjing University, Nanjing 210093, China; College of Engineering and Applied Sciences and Jiangsu Key Laboratory of Artificial Functional Materials, Nanjing University, Nanjing 210093, China*

Pengcheng Huo − *National Laboratory of Solid-State Microstructures and Collaborative Innovation Center of Advanced Microstructures, Nanjing University, Nanjing 210093, China; College of Engineering and Applied Sciences*

and Jiangsu Key Laboratory of Artificial Functional Materials, Nanjing University, Nanjing 210093, China

Mingze Liu − *National Laboratory of Solid-State Microstructures and Collaborative Innovation Center of Advanced Microstructures, Nanjing University, Nanjing 210093, China; College of Engineering and Applied Sciences and Jiangsu Key Laboratory of Artificial Functional Materials, Nanjing University, Nanjing 210093, China*

Wenqi Zhu − *Physical Measurement Laboratory, National Institute of Standards and Technology, Gaithersburg, Maryland 20899, United States; Maryland NanoCenter, University of Maryland, College Park, Maryland 20742, United States;* orcid.org/0000-0001-7832-189X

Amit Agrawal − *Physical Measurement Laboratory, National Institute of Standards and Technology, Gaithersburg, Maryland 20899, United States; Maryland NanoCenter, University of Maryland, College Park, Maryland 20742, United States;* orcid.org/0000-0002-9619-7623

Complete contact information is available at:
https://pubs.acs.org/10.1021/acs.nanolett.2c03822

Author Contributions

R.Y., P.H., and M.L. equally contributed to this work. R.Y., P.H., and M.L. performed the theoretical design, numerical simulations, and experimental measurements. All authors contributed toward the interpretation of results and participated in manuscript preparation. T.X. directed the project.

Notes

The authors declare no competing financial interest.

ACKNOWLEDGMENTS

REFERENCES

(1) Harris, J.; Grillo, V.; Mafakheri, E.; Gazzadi, G. C.; Frabboni, S.; Boyd, R. W.; Karimi, E. Structured quantum waves. *Nat. Phys.* **2015**, *11*, 629−634.

(2) Lloyd, S. M.; Babiker, M.; Thirunavukkarasu, G.; Yuan, J. Electron vortices: Beams with orbital angular momentum. *Rev. Mod. Phys.* **2017**, *89*, 035004.

(3) Bliokh, K. Y.; Ivanov, I. P.; Guzzinati, G.; Clark, L.; Van Boxem, R.; Beche, A.; Juchtmans, R.; Alonso, M. A.; Schattschneider, P.; Nori, F.; Verbeeck, J. Theory and applications of free-electron vortex states. *Phys. Rep.* **2017**, *690*, 1−70.

(4) Bliokh, K. Y.; Bliokh, Y. P.; Savel'ev, S.; Nori, F. Semiclassical dynamics of electron wave packet states with phase vortices. *Phys. Rev. Lett.* **2007**, *99*, 190404.

(5) Uchida, M.; Tonomura, A. Generation of electron beams carrying orbital angular momentum. *Nature* **2010**, *464*, 737−739.

(6) Verbeeck, J.; Tian, H.; Schattschneider, P. Production and application of electron vortex beams. *Nature* **2010**, *467*, 301−304.

(7) McMorran, B. J.; Agrawal, A.; Anderson, I. M.; Herzing, A. A.; Lezec, H. J.; McClelland, J. J.; Unguris, J. Electron vortex beams with high quanta of orbital angular momentum. *Science* **2011**, *331*, 192−195.

(8) Grillo, V.; Gazzadi, G. C.; Karimi, E.; Mafakheri, E.; Boyd, R. W.; Frabboni, S. Highly efficient electron vortex beams generated by nanofabricated phase holograms. *Appl. Phys. Lett.* **2014**, *104*, 043108.

(9) Edström, A.; Lubk, A.; Rusz, J. Elastic scattering of electron vortex beams in magnetic matter. *Phys. Rev. Lett.* **2016**, *116*, 127203.

(10) Yang, Y.; Thirunavukkarasu, G.; Babiker, M.; Yuan, J. Orbital-angular-momentum mode selection by rotationally symmetric super-

position of chiral states with application to electron vortex beams. *Phys. Rev. Lett.* **2017**, *119*, 094802.

(11) Pozzi, G.; Lu, P.; Tavabi, A. H.; Duchamp, M.; Dunin-Borkowski, R. E. Generation of electron vortex beams using line charges via the electrostatic Aharonov-Bohm effect. *Ultramicroscopy* **2017**, *181*, 191−196.

(12) Verbeeck, J.; Beche, A.; Muller-Caspary, K.; Guzzinati, G.; Luong, M. A.; Hertog, M. D. Demonstration of a 2 × 2 programmable phase plate for electrons. *Ultramicroscopy* **2018**, *190*, 58−65.

(13) Schattschneider, P.; Stöger-Pollach, M.; Verbeeck, J. Novel vortex generator and mode converter for electron beams. *Phys. Rev. Lett.* **2012**, *109*, 084801.

(14) Guzzinati, G.; Beche, A.; Lourenco-Martins, H.; Martin, J.; Kociak, M.; Verbeeck, J. Probing the symmetry of the potential of localized surface plasmon resonances with phase-shaped electron beams. *Nat. Commun.* **2017**, *8*, 14999.

(15) Voloch-Bloch, N.; Lereah, Y.; Lilach, Y.; Gover, A.; Arie, A. Generation of electron Airy beams. *Nature* **2013**, *494*, 331−335.

(16) Shiloh, R.; Tsur, Y.; Remez, R.; Lereah, Y.; Malomed, B. A.; Shvedov, V.; Hnatovsky, C.; Krolikowski, W.; Arie, A. Unveiling the orbital angular momentum and acceleration of electron beams. *Phys. Rev. Lett.* **2015**, *114*, 096102.

(17) Grillo, V.; Karimi, E.; Gazzadi, G. C.; Frabboni, S.; Dennis, M. R.; Boyd, R. W. Generation of nondiffracting electron Bessel beams. *Phys. Rev. X* **2014**, *4*, 011013.

(18) Zheng, C.; Petersen, T. C.; Kirmse, H.; Neumann, W.; Morgan, M. J.; Etheridge, J. Axicon lens for electrons using a magnetic vortex: The efficient generation of a Bessel beam. *Phys. Rev. Lett.* **2017**, *119*, 174801.

(19) Mutzafi, M.; Kaminer, I.; Harari, G.; Segev, M. Non-diffracting multi-electron vortex beams balancing their electron-electron interactions. *Nat. Commun.* **2017**, *8*, 650.

(20) Polman, A.; Kociak, M.; García de Abajo, F. J. Electron beam spectroscopy for nanophotonics. *Nat. Mater.* **2019**, *18*, 1158−1171.

(21) Coullet, P.; Gil, L.; Rocca, F. Optical vortices. *Opt. Commun.* **1989**, *73*, 403−408.

(22) Allen, L.; Beijersbergen, M. W.; Spreeuw, R. J. C.; Woerdman, J. P. Orbital angular momentum of light and the transformation of Laguerre-Gaussian Laser modes. *Phys. Rev. A* **1992**, *45*, 8185−8189.

(23) Pu, M.; Li, X.; Ma, X.; Wang, Y.; Zhao, Z.; Wang, C.; Hu, C.; Cao, P.; Huang, C.; Ren, H.; Li, X.; Qin, F.; Yang, J.; Gu, M.; Hong, M.; Luo, X. Catenary optics for achromatic generation of perfect optical angular momentum. *Sci. Adv.* **2015**, *1*, No. e1500396.

(24) Ren, H.; Li, X.; Zhang, Q.; Gu, M. On-chip noninterference angular momentum multiplexing of broadband light. *Science* **2016**, *352*, 805−809.

(25) Ma, Q.; Shi, C.; Bai, G.; Chen, T.; Noor, A.; Cui, T. J. Beam-editing coding metasurfaces based on polarization bit and orbital angular momentum mode bit. *Adv. Opt. Mater.* **2017**, *5*, 1700548.

(26) Tan, Q.; Guo, Q.; Liu, H.; Huang, X.; Zhang, S. Controlling plasmonic orbital angular momentum by combining geometric and dynamic phase. *Nanoscale* **2017**, *9*, 4944−4949.

(27) Huang, K.; Liu, H.; Restuccia, S.; Mehmood, M. Q.; Mei, S.; Giovannini, D.; Danner, A.; Padgett, M. J.; Teng, J. H.; Qiu, C. W. Spiniform phase-encoded metagratings entangling arbitrary rational-order orbital angular momentum. *Light: Sci. & Appl.* **2018**, *7*, 17156.

(28) Shen, Y.; Wang, X.; Xie, Z.; Min, C.; Fu, X.; Liu, Q.; Gong, M.; Yuan, X. Optical vortices 30 years on: OAM manipulation from topological charge to multiple singularities. *Light: Sci. & Appl.* **2019**, *8*, 90.

(29) Ivanov, I. P.; Karlovets, D. V. Detecting transition radiation from a magnetic moment. *Phys. Rev. Lett.* **2013**, *110*, 264801.

(30) Asenjo-Garcia, A.; Garcia de Abajo, F. J. Dichroism in the interaction between vortex electron beams, plasmons, and molecules. *Phys. Rev. Lett.* **2014**, *113*, 066102.

(31) Ostrovsky, A. S.; Rickenstorff-Parrao, C.; Arrizon, V. Generation of the "perfect" optical vortex using a liquid-crystal spatial light modulator. *Opt. Lett.* **2013**, *38*, 534−536.

(32) Vaity, P.; Rusch, L. Perfect vortex beam: Fourier transformation of Bessel Beam. *Opt. Lett.* **2015**, *40*, 597.

(33) Zhang, C.; Min, C.; Du, L.; Yuan, X. Perfect optical vortex enhanced surface plasmon excitation for plasmonic structured illumination microscopy imaging. *Appl. Phys. Lett.* **2016**, *108*, 201601.

(34) Zhang, Y.; Liu, W.; Gao, J.; Yang, X. Generating focused 3D perfect vortex beams By plasmonic metasurfaces. *Adv. Opt. Mater.* **2018**, *6*, 1701228.

(35) Bao, Y.; Ni, J.; Qiu, C. A minimalist single-layer metasurface for arbitrary and full control of vector vortex beams. *Adv. Mater.* **2020**, *32*, No. e1905659.

(36) Han, J.; Intaravanne, Y.; Ma, A.; Wang, R.; Li, S.; Li, Z.; Chen, S.; Li, J.; Chen, X. Optical metasurfaces for generation and superposition of optical ring vortex beams. *Laser Photonics Rev.* **2020**, *14*, 2000146.

(37) Durnin, J.; Miceli, J. J., Jr.; Eberly, J. H. Diffraction-free beams. *Phys. Rev. Lett.* **1987**, *58*, 1499.

(38) McGloin, D.; Dholakia, K. Bessel beams: Diffraction in a new light. *Contemp. Phys.* **2005**, *46*, 15−28.

(39) Bliokh, K. Y.; Schattschneider, P.; Verbeeck, J.; Nori, F. Electron vortex beams in a magnetic field: A new twist on landau levels and Aharonov-Bohm states. *Phys. Rev. X* **2012**, *2*, 041011.

(40) Gori, F.; Guattari, G.; Padovani, C. Bessel-Gauss beams. *Opt. Commun.* **1987**, *64*, 491−495.

(41) Thirunavukkarasu, G.; Mosley, M.; Babiker, M.; Yuan, J. Normal modes and mode transformation of pure electron vortex beams. *Philosophical Transactions A* **2017**, *375*, 20150438.

(42) Harvey, T. R.; Pierce, J. S.; Agrawal, A. K.; Ercius, P.; Linck, M.; McMorran, B. J. Efficient diffractive phase optics for electrons. *New J. Phys.* **2014**, *16*, 093039.

(43) Rusz, J.; Bhowmick, S. Boundaries for efficient use of electron vortex beams to measure magnetic properties. *Phys. Rev. Lett.* **2013**, *111*, 105504.

(44) Grillo, V.; Harvey, T. R.; Venturi, F.; Pierce, J. S.; Ballboni, R.; Bouchard, F.; Gazzadi, G. C.; Frabboni, S.; Tavabi, A. H.; Li, Z.; Dunin-Borkowski, R. E.; Boyd, R. W.; McMorran, B. J.; Karimi, E. Observation of nanoscale magnetic fields using twisted electron beams. *Nat. Commun.* **2017**, *8*, 689.

(45) Ivanov, I. P.; Karlovets, D. V. Polarization radiation of vortex electrons with large orbital angular momentum. *Phys. Rev. A* **2013**, *88*, 043840.

(46) Schattschneider, P.; Schachinger, T.; Stoger-Pollach, M.; Loffler, S.; Steiger-Thirsfeld, A.; Bliokh, K. Y.; Nori, F. Imaging the dynamics of free-electron Landau states. *Nat. Commun.* **2014**, *5*, 4586.

(47) Guzzinati, G.; Schattschneider, P.; Bliokh, K. Y.; Nori, F.; Verbeeck, J. Observation of the Larmor and Gouy rotations with electron vortex beams. *Phys. Rev. Lett.* **2013**, *110*, 093601.

(48) Bliokh, K. Y.; Dennis, M. R.; Nori, F. Relativistic electron vortex beams: angular momentum and spin-orbit interaction. *Phys. Rev. Lett.* **2011**, *107*, 174802.

(49) Bliokh, K. Y.; Nori, F. Spatiotemporal vortex beams and angular momentum. *Phys. Rev. A* **2012**, *86*, 033824.

(50) Bliokh, K. Y.; Dennis, M. R.; Nori, F. Position, spin, and orbital angular momentum of a relativistic electron. *Phys. Rev. A* **2017**, *96*, 023622.

(51) Shiloh, R.; Lereah, Y.; Lilach, Y.; Arie, A. Sculpturing the electron wave function using nanoscale phase masks. *Ultramicroscopy* **2014**, *144*, 26−31.